

# Photodissociation of Nitrosobenzene and Decomposition of Phenyl Radical<sup>†</sup>

Cheng-Ming Tseng,<sup>‡</sup> Y. M. Choi,<sup>§</sup> Cheng-Liang Huang,<sup>‡,||</sup> Chi-Kung Ni,<sup>\*,‡</sup> Yuan T. Lee,<sup>‡,⊥</sup> and M. C. Lin<sup>\*,§,∇</sup>

*Institute of Atomic and Molecular Sciences, Academia Sinica, Post Office Box 23-166, Taipei, Taiwan, Department of Chemistry, Emory University, Atlanta, Georgia 30322, Department of Chemistry, National Taiwan University, Taipei, 106, Taiwan, and Center for Interdisciplinary Molecular Science, National Chiao Tung University, Hsinchu 300, Taiwan*

Received: February 9, 2004; In Final Form: March 23, 2004

Photodissociation of nitrosobenzene in a molecular beam has been studied by multimass ion imaging techniques. Photodissociation at 248 nm shows that there is only one dissociation channel, i.e.,  $C_6H_5NO \rightarrow C_6H_5 + NO$ , regardless of the fact that the other channel,  $C_6H_5NO \rightarrow C_6H_4 + HNO$ , is energetically accessible in agreement with theoretically predicted results. Photodissociation at 193 nm also shows the same dissociation channel. However, about 10% of the  $C_6H_5$  radicals produced at this wavelength further decomposed into benzyne and H atom, and the dissociation rates of phenyl radical as a function of internal energies were measured. The averaged photofragment translational energies released from the dissociation of nitrosobenzene at 193 and 248 nm are 10.2 and 6.9 kcal/mol, respectively, and fragment distributions are almost isotropic at both wavelengths. In addition, the thermal rate constant for dissociation of  $C_6H_5NO$  has been computed and compared with experimental data; the agreement between theory and experiment is excellent, confirming the most recently reported unusually high A-factor ( $> 10^{17} \text{ s}^{-1}$ ).

## I. Introduction

Nitrosobenzene has been popularly employed photolytically as the precursor of phenyl radicals in many kinetic and spectroscopic studies because of its large extinction coefficient in the UV region.<sup>1–8</sup> The molecule has a large energy gap between the  $S_1$  and  $S_2$  states.<sup>9,10</sup> Hence, the possibility of fluorescence from the  $S_2$  state has been discussed.<sup>11</sup> However, no fluorescence has been observed.<sup>12–14</sup> The existence of a fast decay channel in the  $S_2$  state is therefore expected. Indeed, it was found that the dissociation of nitrosobenzene in argon matrices at 12 K is very efficient upon irradiation of UV photons.<sup>15</sup>

The dynamics of photodissociation of nitrosobenzene in the gas phase have been studied recently.<sup>16–22</sup> However, conclusions are very different from these studies. Dick and co-workers<sup>17</sup> measured the absorption spectrum of the  $S_0 - S_2$  transition of the ultracold nitrosobenzene in a supersonic jet. A lifetime of the  $S_2$  state determined directly by the homogeneous line width of the absorption spectrum was found to be  $60 \pm 3$  fs. They also measured the alignment, velocity distribution, and populations of the rotational and vibrational states of the NO fragments via laser-induced fluorescence and ion imaging technique at various UV wavelengths.<sup>18–20</sup> Fragments have an isotropic velocity distribution and no alignment was observed. In addition, the NO rotational population has a statistical distribution and only 10% of the NO fragments are produced in vibrational

excited states. They concluded that the primarily populated  $S_n$  state ( $n \geq 2$ ) decays rapidly through internal conversion to the  $S_1$  or  $S_0$  state, and the dissociation occurs through a statistical mechanism on the potential surface of the lower state on a time scale much slower than rotation of the parent molecule. On the other hand, Han and co-workers<sup>21,22</sup> also have studied the photodissociation of nitrosobenzene at 266 nm recently. The anisotropy parameter  $\beta = -0.64$  was found from the time-of-flight spectra of NO and  $C_6H_5$  photofragments. Their laser-induced fluorescence study also demonstrated that more than 60% of the NO fragments are populated in the vibrational excited state and the NO fragment rotational temperature is much higher than that measured by Dick et al.

In all existing studies, including those kinetic and spectroscopic papers cited above, only one dissociation channel,  $C_6H_5NO \rightarrow C_6H_5 + NO$ , has been assumed and/or detected in the photodissociation of nitrosobenzene in the UV region, despite the fact that the  $C_6H_4 + HNO$  product channel is accessible at 248 nm while the  $C_6H_4 + H + NO$  product channel becomes energetically accessible at 193 nm.

In this report, photodissociation of nitrosobenzene at 193 and 248 nm was studied by multimass ion imaging techniques. Particular attention has been focused on the search for the other possible dissociation channel and the fragment anisotropy measurement. In addition, the decomposition of the phenyl radical produced from the photodissociation reaction and the thermal decomposition of nitrosobenzene were also studied; the data will be discussed in reference to the ab initio MO and statistical theory results.

## II. Experimental Section

**Experimental Setup.** The experimental techniques have been described in detail in our previous reports on other aromatic molecules,<sup>23–26</sup> and only a brief description is given here.

<sup>†</sup> Part of the special issue "Richard Bersohn Memorial Issue".

\* To whom correspondence may be addressed. E-mail: ckni@po.iams.sinica.edu.tw (C.-K.N.); chemmcl@emory.edu (M.C.L.).

<sup>‡</sup> Academia Sinica.

<sup>§</sup> Emory University.

<sup>||</sup> Present address: Department of Applied Chemistry, National Chiayi University, Chiayi, Taiwan.

<sup>⊥</sup> National Taiwan University.

<sup>∇</sup> National Chiao Tung University.

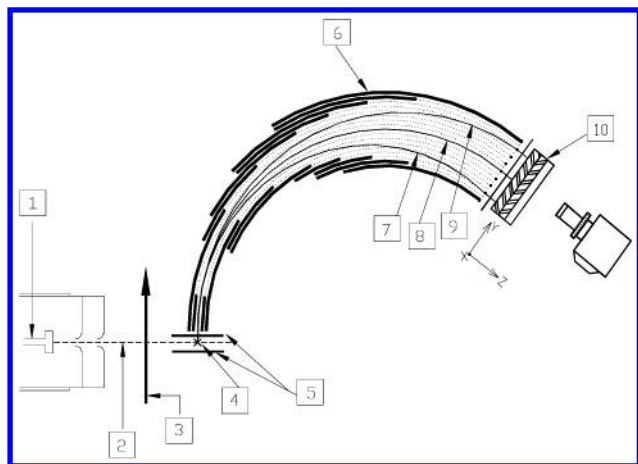


**Figure 1.** Schematic diagram of the multimass ion imaging detection system: (1) nozzle; (2) molecular beam; (3) photolysis laser beam; (4) VUV laser beam, which is perpendicular to the plane of the paper; (5) ion extraction plates; (6) energy analyzer; (7–9) simulation ion trajectories of  $m/e = 16, 14,$  and  $12$ ; (10) two-dimensional detector, where the  $y$ -axis is the mass axis, and the  $x$ -axis (perpendicular to the plane of the paper) is the velocity axis.

Nitrosobenzene vapor was formed by flowing ultrapure He at pressures of 500 Torr through a reservoir filled with sample at 293 K. The nitrosobenzene/He mixture was then expanded through a 500  $\mu\text{m}$  pulsed nozzle to form the molecular beam. Molecules in the molecular beam were photodissociated by an UV laser pulse. Due to the recoil velocity and center-of-mass velocity, the fragments were expanded to a larger sphere on their flight to the ionization region and then ionized by a VUV laser pulse. The distance and time delay between the VUV laser pulse and the UV photolysis laser pulse were set such that the VUV laser beam passed through the center-of-mass of the dissociation products and generated a line segment of photo-fragment ions by photoionization. The length of the segment was proportional to the fragment recoil velocity in the center-of-mass frame multiplied by the delay time between the photolysis and the ionization laser pulses. To separate the different masses within the ion segment, a pulsed electric field was used to extract the ions into a mass spectrometer after ionization. While the mass analysis was being executed in the mass spectrometer, the length of each fragment ion segment continued to expand in the original direction according to its recoil velocity. At the exit port of the mass spectrometer, a two-dimensional ion detector was used to detect the ion positions and intensity distribution. In this two-dimensional detector, one direction was the recoil velocity axis and the other was the mass axis. The schematic diagram of the experimental setup is shown in Figure 1.

**Computational Method.** The hybrid density functional B3LYP<sup>27–29</sup> with three split valence basis sets, 6-31G(d), 6-31+G(d), and 6-31G(2df,p), has been applied to optimize the geometries of the reactant, intermediate, transition state, and products with tight convergence criteria. All the stationary points were identified by the number of imaginary frequencies (NIMG) with NIMG = 0 for stable species and NIMG = 1 for transition states, as well as by the normal-mode analysis. To continue to study the unimolecular reaction of  $\text{C}_6\text{H}_5\text{NO}$  based on our earlier work<sup>30</sup> at the G2M(rcc, MP2) and G2M(RCC, MP2) levels,<sup>31</sup> in this report we also performed quantum-chemical calculations with the G2M(RCC, MP2) scheme. A series of single-point energy calculations for the G2M(RCC, MP2) composite scheme using the geometries and zero-point energy (ZPE) corrections from the B3LYP/6-31G(d) and B3LYP/6-31+G(d) levels of

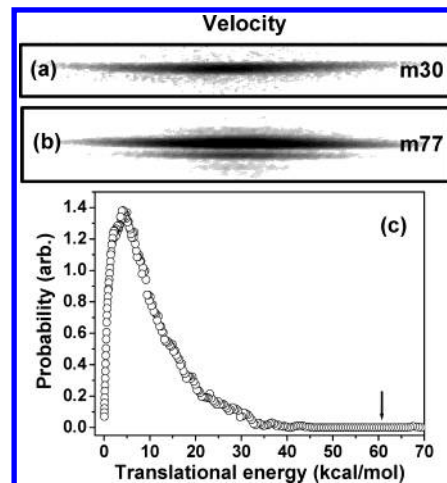


**Figure 2.** Photofragment ion image of (a)  $m/e = 30$ , (b)  $m/e = 77$  and 78, and (c) photofragment translational energy distribution at 248 nm. Arrow indicates the maximum available energy.

theory have been carried out to obtain more reliable information on energetics for the potential energy surface (PES) and the rate constant prediction by

$$E_0[\text{G2M}] = \text{RCCSD(T)/6-311G(d,p)} + \text{MP2/6-311+G(3df,2p)} - \text{MP2/6-311G(d,p)} + \Delta\text{HLC} + \text{ZPE}$$

The empirical  $\Delta\text{HLC}$  is given by  $-5.3n_\beta - 0.19n_\alpha$  in millihartrees, where  $n_\alpha$  and  $n_\beta$  are the numbers of  $\alpha$  and  $\beta$  valence electrons, respectively. Some of the energies have also been calculated by the G3SX composite method<sup>32</sup> with the geometries optimized at the B3LYP/6-31G(2df,p) level. Since the method does not include any empirical correction, this method has been proposed to apply for the system whose number of spins is changed like the present system. Therefore, we can compare the two composite schemes for the issue on the spin change. In addition, time-dependent density functional theory (TD-DFT)<sup>33–35</sup> at the B3LYP/6-31+G(d) level has been used to calculate the vertical excitation energies and oscillator strengths for the  $S_1$  and  $S_2$  states of  $\text{C}_6\text{H}_5\text{NO}$ . The electronic structure calculations were carried out with the Gaussian 98<sup>36</sup> and MOLPRO 98<sup>37</sup> programs.

### III. Results and Discussion

**Dissociation of Nitrosobenzene at 248 nm.** Ions of  $m/e = 30, 77,$  and  $78$  were the only fragments we observed from the photodissociation of nitrosobenzene at this wavelength.  $m/e = 78$  is the corresponding  $^{13}\text{C}$  isotope of fragment  $m/e = 77$ . Photofragment ion images are shown in Figure 2a,b. Photolysis laser intensity in the region between 2.5 and 30  $\text{mJ}/\text{cm}^2$  was used. They showed the same shapes of image. It suggests that one-photon absorption is the dominant process in this laser intensity region. Since there was no  $\text{HNO}$  and  $\text{C}_6\text{H}_4$  detected, we can conclude that there is only one dissociation channel at 248 nm, i.e.,  $\text{C}_6\text{H}_5\text{NO} \rightarrow \text{C}_6\text{H}_5 + \text{NO}$ , although the other channel,  $\text{C}_6\text{H}_5\text{NO} \rightarrow \text{C}_6\text{H}_4 + \text{HNO}$ , is also energetically accessible (vide infra). As a result, nitrosobenzene is a “clean” precursor to generate phenyl radical at this wavelength.

The photofragment translational energy distribution obtained from the images is illustrated in Figure 2c. It shows that the probability monotonically decreases with increasing translational energy. The average released translational energy is about 6.9 kcal/mol, and it is about 11% of the total available energy.

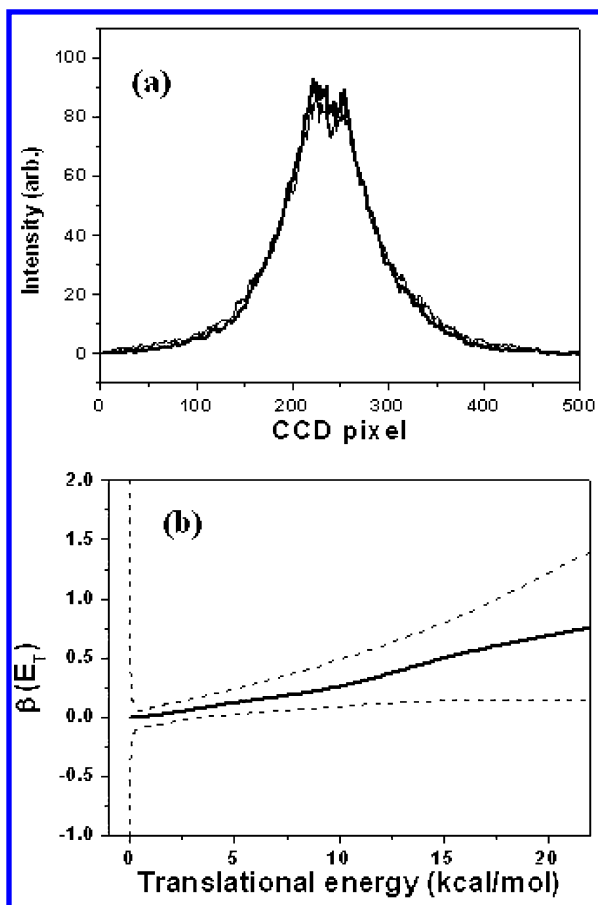


**Figure 3.** (a) Photofragment ion image intensity profiles of  $m/e = 77$  from two different photolysis laser polarizations at 248 nm. Thick and thin lines represent the polarization of UV laser perpendicular and parallel to the VUV laser beam, respectively. (b) Anisotropy parameter  $\beta$  as a function of fragment translational energy. The dotted lines represent the upper and lower limits of the uncertainty.

Compared to the average translational energy measured in previous studies, our value is much smaller than 29% of the fragment translational spectroscopy measurement at photolysis wavelength 266 nm,<sup>22</sup> and it is very close to 7.3% and 6~11% of velocity map ion imaging measurements at 290.5 and 225.96 nm, respectively.<sup>20</sup>

The  $C_6H_5$  photofragment ion image profiles at two different photolysis laser polarizations are presented in Figure 3a. The shapes and the intensities of the profiles at the polarization directions parallel and perpendicular to the VUV probe laser beam are very close to each other. The anisotropy parameter  $\beta$  for the fragments with different translational energy is illustrated in Figure 3b. In the low translational energy region where most of the fragments are produced, the values of  $\beta$  are very close to zero, indicating the isotropic distribution of the fragments. In the high translational energy region, the values of  $\beta$  fluctuate between 0 and 1. The poor S/N ratios are due to the small amount of high translational energy fragments produced in the high translational energy region. We can conclude that most of the fragments are isotropically distributed. If there is any anisotropic distribution, it must be from the fragments with large translational energy. However, the amount of those fragments is very small, and the value of  $\beta$  is positive.

The anisotropy parameter  $\beta$  we measured at 248 nm is very close to the value of 0.05 from the single line measurement at 225.96 nm.<sup>20</sup> It is also very close to the value of 0.03~-0.05 from the measurement of several rotational states of NO  $v = 0$  at photolysis wavelength 290.5 nm.<sup>20</sup> However, it is very

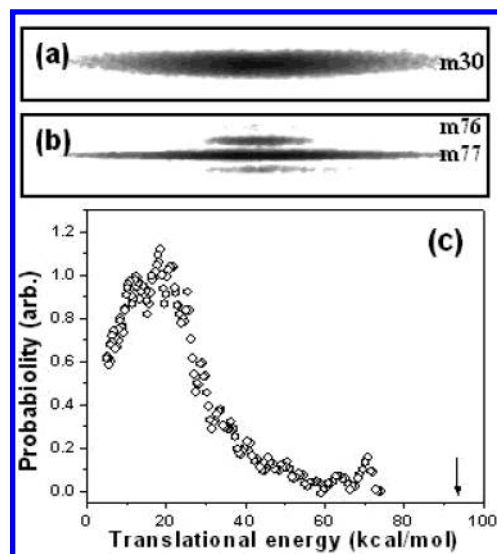


**Figure 4.** Photofragment ion image of (a)  $m/e = 30$ , (b)  $m/e = 76$ , 77, and 78, and (c) photofragment translational energy distribution at 193 nm. Arrow indicates the maximum available energy.

different from the value of  $-0.64$  obtained from the photofragment translational energy measurement at 266 nm.<sup>22</sup> Both the translational energy distribution and anisotropy parameter  $\beta$  measurement suggest that our results are similar to those of Dick and co-workers, but they are different from those of Han and co-workers.

**Dissociation of Nitrosobenzene at 193 nm.** Fragment ions of  $m/e = 30$ , 76, 77, and 78 were observed from the photodissociation of  $C_6H_5NO$  at 193 nm. Photolysis laser intensity in the region between 0.2 and 1.7 mJ/cm<sup>2</sup> were used, and all of these fragment intensities showed linear dependence on the laser intensity. The images are shown in Figure 4. As the delay time between pump and probe laser pulses increased, the relative intensity between  $m/e = 76$  and 77 also changed, as shown in Figure 5. Since no HNO fragment was detected, fragments of  $m/e = 76$  must result from the slow dissociation of the energetic fragments  $m/e = 77$ . Consequently, we can conclude that there is still only one dissociation channel of nitrosobenzene at 193 nm, even though the photon energy is much higher than the dissociation barrier of  $C_6H_5NO \rightarrow C_6H_4 + HNO$ . This observation is consistent with the significantly smaller decay rate predicted for this product channel, as will be presented later. The photofragment translational energy distribution obtained at this wavelength is shown in Figure 4c. The average energy released is 10.2 kcal/mol, which is slightly larger than that at 248 nm.

The anisotropy parameter  $\beta$  at 193 nm was found to be very similar to that at 248 nm. The  $C_6H_5$  photofragment ion image intensity profiles at two different photolysis laser polarizations were found to be very close to each other, as presented in Figure 6a. The values of  $\beta$  as a function of translational energy are shown in Figure 6b. It suggests that most of the fragments are isotropically distributed, and only a small amount of fragments with large translational energy have a positive value of  $\beta$ . The dissociation mechanism at 193 nm must be similar to that at 248 nm.

**Decomposition of Phenyl Radical.** The phenyl radical plays a very important role in the combustion of small aromatic hydrocarbons.<sup>38-40</sup> There has been considerable interest in its reactions with combustion species as well as its decomposition kinetics and mechanism. The ab initio calculation of a previous study<sup>41</sup> showed that the decomposition of phenyl radical

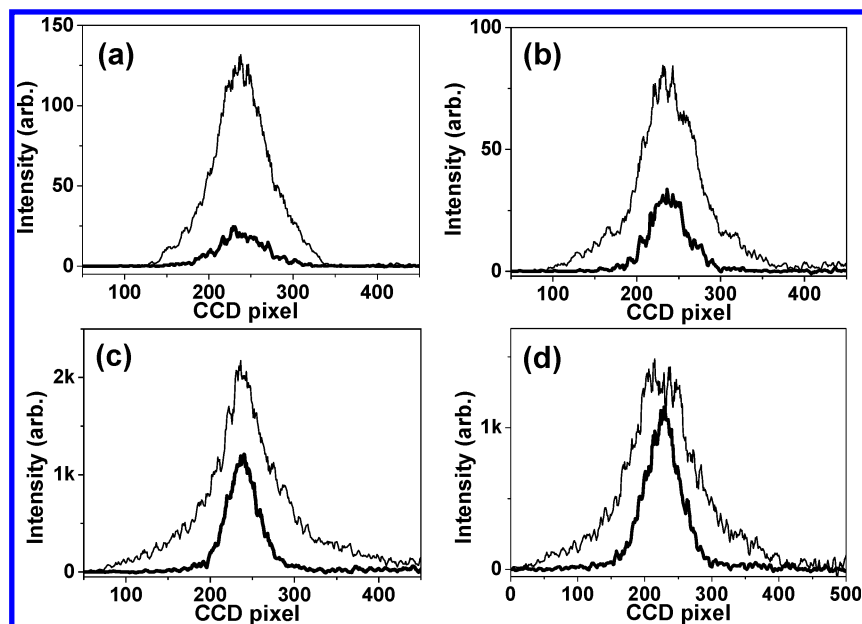


**Figure 5.** Fragment ion image intensity profiles at various delay times. The thin and thick lines represent  $m/e = 77$  and  $76$ , respectively. (a)  $t = 5 \mu\text{s}$ , (b)  $t = 9 \mu\text{s}$ , (c)  $t = 15 \mu\text{s}$ , (d)  $t = 18 \mu\text{s}$ .

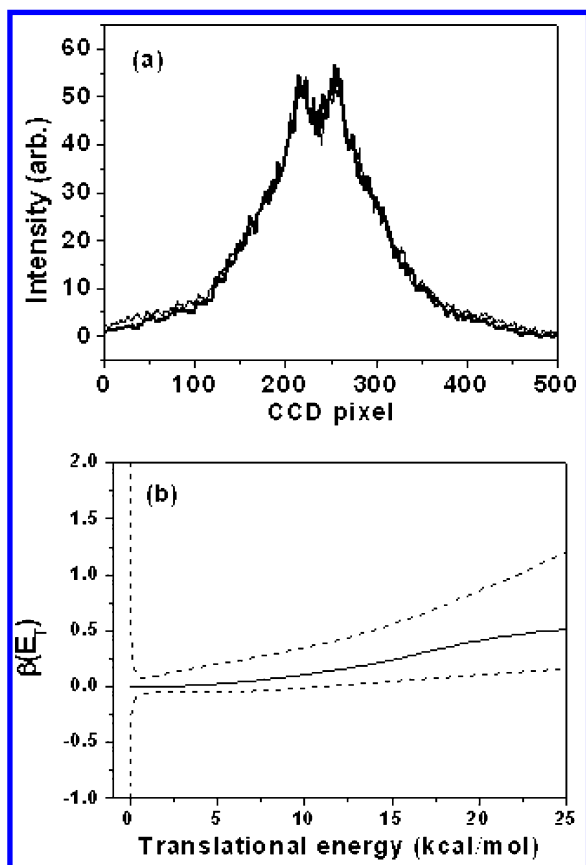


**Figure 6.** (a) Photofragment ion image intensity profiles of  $m/e = 77$  from two different photolysis laser polarizations at 193 nm. Thick and thin lines represent the polarization of UV laser perpendicular and parallel to the VUV laser beam, respectively. (b) Anisotropy parameter  $\beta$  as a function of fragment translational energy. The dotted lines represent the upper and lower limits of the uncertainty.

producing benzyne + H was endothermic by 76.0 kcal/mol, and the reaction was reported to occur without a distinct transition state based on geometry optimization with the B3LYP method. This loose structure, also confirmed by MP2 and CCSD optimizations with the 6-31+G(d,p) basis set, however, overestimated the high-temperature thermal decomposition rate

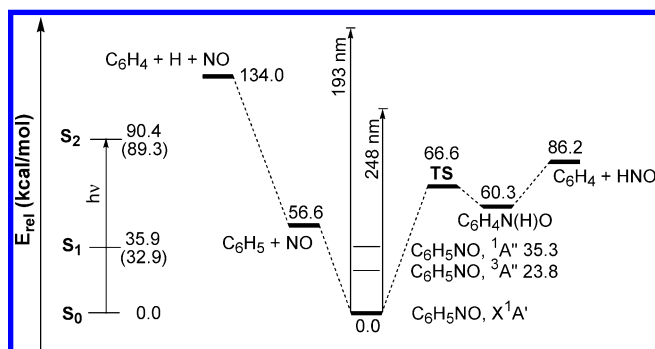


**Figure 7.** Energy level scheme from the TD-DFT calculations at the B3LYP/6-31+G(d) level and schematic energy diagram for the isomerization and dissociation reactions of  $\text{C}_6\text{H}_5\text{NO}$  calculated at the G2M(RCC, MP2)//B3LYP/6-31+G(d) level in kilocalories per mole. Note that the energy of the  $^1\text{A}''$  state, 35.3 kcal/mol, includes ZPE correction. The energy levels in parentheses are from ref 18.

constant determined by Braun-Unkoff et al.,<sup>42</sup> as was also shown by Wang et al.<sup>43</sup> The new optimization carried out in this work by the G96LYP/6-31+G(d,p) method located a low-energy transition state. A G2M calculation based on this structure gives the barrier for the decomposition reaction at 79.4 kcal/mol above  $\text{C}_6\text{H}_5$ . For phenyl radicals produced from the photodissociation of nitrosobenzene at 193 nm, the maximum internal energy for phenyl radical is 93.8 kcal/mol (experimental value from NIST chemistry webbook). The decomposition into benzyne + H therefore is energetically allowed, as shown in Figure 7.

The decomposition of phenyl radical into benzyne and H atom can be clearly seen from the image intensity changes of  $m/e = 77$  and  $76$  at various delay times, as shown in Figure 5. The central part of the fragment images in the velocity axis corresponds to small translational energy released, i.e., most of the available energy is distributed in the fragments' internal degrees of freedom. For the phenyl radicals located at the central part of the image, they contain a lot of internal energy and quickly decompose into benzyne and H atom. Since the mass ratio between benzyne and H atom is large and the available energy for the decomposition process is small, benzyne produced from this part of phenyl radicals is still located at the same position in the velocity axis. The fast decomposition of this part



of phenyl radicals can be seen from the fast rise of the central part of the image  $m/e = 76$  at short delay time. On the other hand, phenyl radicals located on both sides contain less internal energy, and they have slow decomposition rates. The corresponding benzyne only appears at long delay time images. For the phenyl radicals positioned at both ends of the image in velocity axis, the translational energy released is large and the energy left in the internal degrees of freedom is too small for the radical to be further dissociated into benzyne and H atom. They remain as phenyl radicals and no analogous benzyne is produced. Therefore, the length of the image  $m/e = 76$  is shorter than that of  $m/e = 77$  even at very long delay times.

The decomposition rate of phenyl radical as a function of internal energies can be obtained from the image intensity changes of each part of the image along the fragment velocity axis at various delay times. The internal energy of phenyl radical can be calculated from

$$E(\text{int})_{\text{phenyl}} = h\nu - D_0 - E(\text{tran}) - E(\text{int})_{\text{NO}}$$

The photon energy  $h\nu$  is 148 kcal/mol, the dissociation energy  $D_0$  is 54 kcal/mol,<sup>30</sup> and the amount of translational energy released,  $E(\text{tran})$ , can be calculated directly by use of the fragment velocity obtained from the image. The only uncertainty in this equation is the internal energy of fragment NO. However, a proper estimation of the NO fragment internal energy could be made according to the previous studies and our measurement. Previous studies showed that the rotational and vibrational state distributions of NO fragments are statistical, and most of the energy is located in phenyl radical vibrational degrees of freedom. For example, the average vibrational energy of NO fragment is only 1.3% of the total available energy at photolysis laser wavelength 255 nm, and the rotational energies of both phenyl radical and NO are only 0.2% and 3.7%, respectively due to the transition-state geometry. For nitrosobenzene photodissociation at 193 nm, both the value of anisotropy parameter  $\beta$  and the translational energy distribution suggest that the dissociation mechanism is similar to that at 255 nm, i.e., the dissociation occurs after internal conversion to the lower electronic state. Energy must be redistributed among various vibrational degrees of freedom before dissociation occurs and the energy distribution is statistical. Therefore, we estimated that about 95% of the available energy (total available energy after the subtraction of translational energy) is distributed in phenyl radical vibrational degrees of freedom.

For a given internal energy, the decomposition of phenyl radical into benzyne and H atom can be described by  $m_{77}(T_1) = \exp(-kT_1)$  and the growth of the corresponding benzyne can be described by  $m_{76}(T_1) = 1 - \exp(-kT_1)$ .  $m_{77}(T)$  is the phenyl radical concentration for a given internal energy at delay time  $T$ .  $m_{76}(T)$  is the benzyne concentration produced from the corresponding phenyl radical.  $k$  is the dissociation rate of phenyl radical. The ion intensity of  $m/e = 77$  and 76 thus can be described by

$$I_{77}(T_1) = A(1 - \gamma) \exp(-kT_1) \quad (1)$$

$$I_{76}(T_1) = B[1 - \exp(-kT_1)] + A\gamma \exp(-kT_1) \quad (2)$$

$A$  and  $B$  are the ionization cross sections of fragment mass 77 and 76, respectively.  $\gamma$  is the branching ratio of benzyne produced from the dissociative ionization of phenyl radical, described by

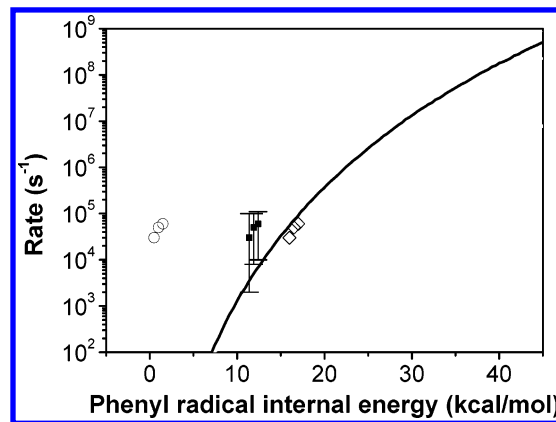
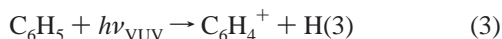


**Figure 8.** Phenyl radical dissociation rate as a function of internal energy. Shown are the experimental values assuming (○) 18%, (■) 5%, and (◇) 0% of the available energy (93 kcal/mol) distributed in NO internal degrees of freedom. The solid line is the prediction at the G2M(RCC, MP2)//G96LYP/6-31+G(d) level in this work.

The dissociation rate can be calculated from the ion intensity ratios of fragment  $m/e = 77$  and 76 at two different delay times by use of

$$\frac{I_{m76}(T_1)}{I_{m77}(T_1)} = \frac{B(1 - e^{-kT_1}) + A\gamma e^{-kT_1}}{A(1 - \gamma)e^{-kT_1}} = \frac{I_{m76}(T_2)}{I_{m77}(T_2)} = \frac{B(1 - e^{-kT_2}) + A\gamma e^{-kT_2}}{A(1 - \gamma)e^{-kT_2}} = \frac{\frac{B}{A(1 - \gamma)}(e^{kT_1} - 1) + \frac{\gamma}{1 - \gamma}}{\frac{B}{A(1 - \gamma)}(e^{kT_2} - 1) + \frac{\gamma}{1 - \gamma}} \quad (4)$$

At short delay time when no benzyne is produced from the decomposition of phenyl radical, ion intensity ratio between  $I_{76}$  and  $I_{77}$  is close to the value of  $\gamma/(1 - \gamma)$ . The upper limit of  $\gamma/(1 - \gamma)$  was obtained from the image at the available shortest delay time (5  $\mu\text{s}$ ), and the final result of the decomposition rate  $k$  was calculated from the numerical solution of eq 4. The phenyl radical dissociation rates as a function of internal energy obtained from this equation are shown in Figure 8. It shows that if the translational energy released in the photodissociation of nitrosobenzene is less than 1 kcal/mol, the decomposition rate of corresponding phenyl radical is in the region between  $10^5$  and  $10^4 \text{ s}^{-1}$ . However, if the translational energy release is more than 2 kcal/mol, the decomposition rate is too slow ( $< 10^4 \text{ s}^{-1}$ ) to be measured in our apparatus. The comparison of absolute ion image intensities of  $m/e = 77$  between short and long delay times indicates that about 10% of phenyl radicals decompose into benzyne and H atom within the time scale ( $< 25 \mu\text{s}$ ) of our experiment. Compared to the decomposition rate obtained from G2M(RCC, MP2)//G96LYP/6-31+G(d) ab initio MO and statistical-theory calculations, the agreement between theory and experiment is satisfactory.

#### Theoretical Prediction of $\text{C}_6\text{H}_5\text{NO}$ Decomposition Rates:

(1) *PES of the System.* As described in the preceding section, the potential energy surface of the  $\text{C}_6\text{H}_5\text{NO}$  system has been calculated with the G2M method<sup>31</sup> based on the geometry optimized at the B3LYP/6-31+G(d,p) level of theory. The optimized structures of the reactant, transition state, and intermediate are presented in Figure 9. All the geometries of the  $\text{C}_6\text{H}_5\text{NO}$  ( $S_0$ , X  $^1\text{A}'$ ),  $\text{C}_6\text{H}_5\text{NO}$  ( $T_1$ ,  $^3\text{A}''$ ), and  $\text{C}_6\text{H}_5\text{NO}$  ( $S_1$ ,  $^1\text{A}''$ ) are planar with  $\text{C}_s$  symmetry. The equilibrium C–N bond

**TABLE 1: Relative Energies<sup>a</sup> for the Isomerization and Decomposition Reactions of C<sub>6</sub>H<sub>5</sub>NO**

species or reaction	B3LYP/6-31G(d)	G2M <sup>b</sup>	B3LYP/6-31+G(d)	G2M <sup>c</sup>	B3LYP/6-31G(2df,p)	G3SX <sup>d</sup>
C <sub>6</sub> H <sub>5</sub> NO	0.0	0.0	0.0	0.0	0.0	0.0
C <sub>6</sub> H <sub>5</sub> + NO	53.3	56.5	52.2	56.6	53.0	55.6
TS	66.1	66.7	65.6	66.6	63.3	66.0
C <sub>6</sub> H <sub>4</sub> N(H)O	60.5	60.2	57.8	60.3	58.4	59.6
C <sub>6</sub> H <sub>4</sub> + HNO	96.2	86.2	93.2	86.2	94.8	86.3
C <sub>6</sub> H <sub>4</sub> + H + NO	140.4	134.0	138.4	134.0	140.2	134.1

<sup>a</sup> Relative energies are ZPE-corrected in kilocalories per mole. <sup>b-d</sup> Based on the optimized geometries calculated at B3LYP/6-31G(d), B3LYP/6-31+G(d), and B3LYP/6-31G(2df,p), respectively.

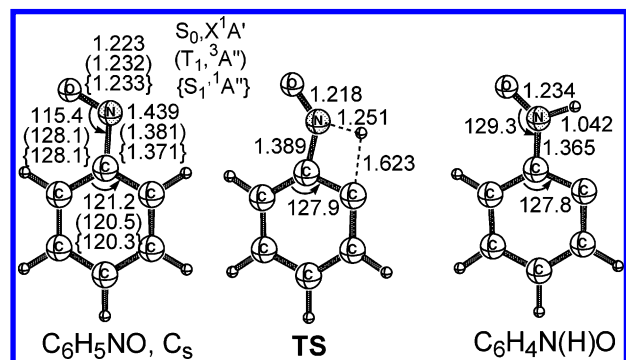


**Figure 9.** Optimized structures of the reactant, transition state, and intermediate at the B3LYP/6-31+G(d) level of theory.

**TABLE 2: Vertical Energies and Oscillator Strengths (*f*) for C<sub>6</sub>H<sub>5</sub>NO, Estimated by TD-DFT at the B3LYP/6-31+(d) Level<sup>a</sup>**

state	sym	B3LYP/6-31+G(d)	experimental <sup>b</sup>
S <sub>1</sub>	1A	35.9 (0.0003)	32.9
S <sub>2</sub>	1A	90.4 (0.0183)	89.3

<sup>a</sup> Vertical energies are given in kilocalories per mole; oscillator strengths are shown in parentheses. <sup>b</sup> From ref 18.

lengths of T<sub>1</sub> and S<sub>1</sub> states are shorter than that of the S<sub>0</sub> state as shown in Figure 9. The predicted energetics and potential energy diagram for the formation of products accessible to 193 nm photon energy are presented in Table 1 and Figure 7, respectively. At the G2M level, the four-centered transition state leading to C<sub>6</sub>H<sub>4</sub> + HNO was predicted to locate at 67 kcal/mol above C<sub>6</sub>H<sub>5</sub>NO, about 19 kcal/mol below the dissociated products. This suggests that a stable molecular complex must exist between C<sub>6</sub>H<sub>5</sub>NO and C<sub>6</sub>H<sub>4</sub> + HNO. A detailed IRC calculation indeed confirms the presence of a benzyne–HNO complex, C<sub>6</sub>H<sub>4</sub>N(H)O, lying 60 kcal/mol above C<sub>6</sub>H<sub>5</sub>NO (see Figure 9 for its structure). Further decomposition of the C<sub>6</sub>H<sub>4</sub>N(H)O complex was found to take place without a well-defined intrinsic barrier, similar to the fragmentation of C<sub>6</sub>H<sub>5</sub>NO to C<sub>6</sub>H<sub>5</sub> and NO.

As shown in Table 1, the energetics predicted by both G2M and G3SX agree very closely. The latter, which does not include “high-level corrections”, is believed to be more reliable for applications to reactions with spin changes. In Table 2, the result of our TD-DFT calculations at the B3LYP/6-31+G(d) level for the S<sub>1</sub> and S<sub>2</sub> states confirms the energy gap between them, 54.5 kcal/mol, which compares closely with the experimental value, 56.4 kcal/mol.<sup>18</sup>

(2) *Decomposition of Photoexcited C<sub>6</sub>H<sub>5</sub>NO.* Assuming that the internal conversion is fast comparing with fragmentation lifetimes, we can predict the fragmentation rates of C<sub>6</sub>H<sub>5</sub>NO following the excitation at 248 and 193 nm on the basis of the RRKM theory. As both product channels giving NO and HNO occur barrierlessly, the energy-dependent specific constants (*k<sub>E</sub>*) were evaluated with the flexible transition state approach<sup>44–47</sup>

**TABLE 3: Decay Rate of C<sub>6</sub>H<sub>5</sub>NO via Different Pathways**

pathway	248 nm	193 nm
C <sub>6</sub> H <sub>5</sub> NO → C <sub>6</sub> H <sub>5</sub> + NO	2.5 × 10 <sup>10</sup>	3.2 × 10 <sup>10</sup>
C <sub>6</sub> H <sub>5</sub> NO → C <sub>6</sub> H <sub>4</sub> + HNO <sup>a</sup>	1.0 × 10 <sup>4</sup>	1.3 × 10 <sup>7</sup>
C <sub>6</sub> H <sub>5</sub> NO → C <sub>6</sub> H <sub>4</sub> N(H)O	2.9 × 10 <sup>5</sup>	1.8 × 10 <sup>7</sup>

<sup>a</sup> The rate constant for C<sub>6</sub>H<sub>5</sub>NO → VTS → C<sub>6</sub>H<sub>4</sub> + HNO with VTS as the limiting step.

by use of the Variflex code.<sup>48</sup> The minimum energy paths (MEP) representing the dissociation processes were approximated with the Varshni potential,<sup>49</sup>  $V(r) = D_e\{-a \exp[-b(R^2 - R_0^2)]\} - D_e$ , where *R* is the reaction coordinate, *R*<sub>0</sub> is the equilibrium value of *R*, *a* = *R*<sub>0</sub>/*R*, and *D<sub>e</sub>* is the bond energy excluding the zero-point energy correction. Along the reaction coordinate, we stretched the bond length of C–N with a step size of 0.2 Å along the path from the equilibrium value to 5 Å. Each geometry was fully optimized at the B3LYP/6-31+G(d) level of theory and its energy was then scaled by the G2M(RCC, MP2) value for the Varshni potential. The approximated bond energy and *b* for the ground state with <sup>1</sup>A' are 60.4 kcal/mol and 0.522 Å<sup>-2</sup>, respectively, for *R*<sub>0</sub> = 1.439 Å. Similar calculations for the dissociation of C<sub>6</sub>H<sub>4</sub>N(H)O, C<sub>6</sub>H<sub>5</sub>NO (T<sub>1</sub>, <sup>3</sup>A'') and C<sub>6</sub>H<sub>5</sub>NO (S<sub>1</sub>, <sup>1</sup>A'') gave rise to *D<sub>e</sub>* = 30.3, 36.0, and 20.0 kcal/mol; *b* = 0.863, 0.834, and 0.991 Å<sup>-2</sup>; and *R*<sub>0</sub> = 1.365, 1.381, and 1.371 Å, respectively.

By use of the molecular parameters given above, the specific rate constants for the dissociation of C<sub>6</sub>H<sub>5</sub>NO at 248 and 193 nm (approximately 115 and 148 kcal/mol, respectively) provide the lifetimes of the excited molecule along various pathways as summarized in Table 3.

The lifetimes of C<sub>6</sub>H<sub>5</sub>NO are predicted to be about 40 ps following the excitation at 248 nm and 33 ps for excitation at 193 nm, producing exclusively C<sub>6</sub>H<sub>5</sub> + NO as was observed experimentally. The formation of HNO, slower by 10<sup>5</sup> at 248 nm and 10<sup>3</sup> at 193 nm, is experimentally undetectable. As the formation of HNO occurs via both the tight four-centered TS1 and the variational TS near the dissociation threshold, with the latter being slightly slower due to its higher energy (see Table 3), we have examined the effect of multiple reflections between the two TSs; the effect was found to be negligible because of the high photon energies. The predicted lifetimes are much longer than that derived from the line width measurement, suggesting that internal conversion is considerably faster than the fragmentation process.

(3) *Thermal Decomposition Rate Constant.* The high-pressure, first-order rate constant for the decomposition of C<sub>6</sub>H<sub>5</sub>NO producing C<sub>6</sub>H<sub>5</sub> + NO,  $k^\infty = (1.42 \pm 0.13) \times 10^{17} \exp[-(55\,060 \pm 1080)/RT] \text{ s}^{-1}$ ,<sup>30</sup> is seen to have an unusually large *A*-factor. The extrapolated rate constants in the temperature range of 800–1000 K from the equation lie between the result of Horn et al.<sup>50</sup> (after high-pressure-limit correction by the RRKM theory) and that of Choo et al.<sup>51</sup> determined by the very-low-pressure pyrolysis method. Theoretically, the rate constant can be computed with the Varshni potential evaluated for the

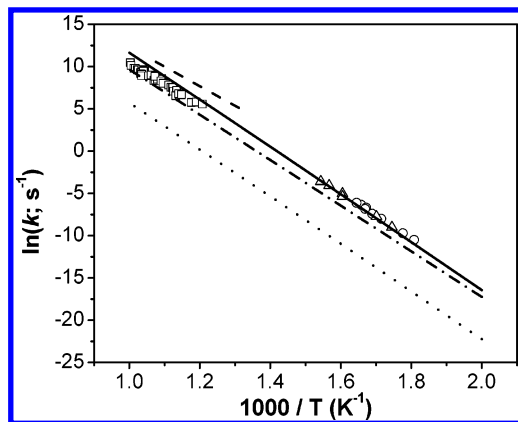


**Figure 10.** Experimental and predicted thermal rate constants for the dissociation of  $C_6H_5NO$  at the high-pressure limit: ( $\square$ ) from ref 50; ( $\Delta$ ) with NO added and ( $\circ$ ) without NO added, from ref 30; (— —) from ref 51. Also shown are predictions for the states of X (—)  $^1A'$ , (— · —)  $^1A''$ , and (···)  $^3A''$ , respectively. Their sum gives  $k^\infty = 1.52 \times 10^{17} \exp[-55200/RT] s^{-1}$ .

three MEPs producing NO. The thermal unimolecular dissociation rate constant defined by

$$d[C_6H_5]/dt = k^\infty [C_6H_5NO]_0 = \sum k_i^\infty X_i = k_X^\infty [X] + k_A^\infty [A] + k_B^\infty [B] \quad (5)$$

where  $[C_6H_5NO]_0$ ,  $[X]$ ,  $[A]$ , and  $[B]$  are, respectively, the initial concentration of nitrosobenzene entirely at its ground electronic state and those at the ground electronic,  $^3A''$ , and  $^1A''$  states under thermal equilibrium, and the  $k_i^\infty$  are the first-order rate constants for the dissociation from these states. Assuming  $K_A$  and  $K_B$  to be the equilibrium constants for  $X \leftrightarrow A$  and  $X \leftrightarrow B$ , respectively, eq 5 leads to the total unimolecular rate constant:

$$k^\infty = (k_X^\infty + k_A^\infty K_A + k_B^\infty K_B) / (1 + K_A + K_B) \quad (6)$$

The predicted individual rate constants presented in Figure 10 gave  $k^\infty = 1.52 \times 10^{17} \exp[-55200/RT] s^{-1}$ , which is in excellent agreement with the result obtained by Park et al.,<sup>30</sup>  $k^\infty = (1.42 \pm 0.13) \times 10^{17} \exp[-(55060 \pm 1080)/RT] s^{-1}$ , confirming the unusually high  $A$ -factor. Notably, the result presented in Figure 10 indicates that the contributions from both  $T_1$  and  $S_1$  states are insignificant in the present system. For the decomposition of  $SO_2$  at high temperatures in shock waves, we have recently shown that contributions from three excited states to its second-order rate constants are significant.<sup>52</sup>

#### IV. Conclusions

We demonstrate that there is only one dissociation channel of nitrosobenzene at both 248 and 193 nm. No products corresponding to the dissociation channel of  $C_6H_5NO \rightarrow C_6H_4 + HNO$  were observed, in full agreement with theoretical prediction. The dissociation rate of nitrosobenzene is on a time scale much longer than the rotation of molecule, and the fragment distribution is almost isotropic. The results at 248 nm are close to the measurement of Dick and co-workers. In addition, about 10% of phenyl radical produced at 193 nm further decompose into benzyne and H atom, and the dissociation rates of phenyl radical as a function of internal energies were measured. The results for the dissociation of the excited  $C_6H_5NO$  and the  $C_6H_5$  radical agree well with theoretically predicted values. In addition, the rate constant for the thermal decomposition of nitrosobenzene has been calculated with variational RRKM theory by including the small contributions

from the two low-lying excited states ( $T_1$  and  $S_1$ ). The agreement between theory and the experiment of Park et al.<sup>30</sup> was also found to be excellent, confirming for the first time the observed very high  $A$ -factor ( $>10^{17} s^{-1}$ ).

**Acknowledgment.** C.K.N. acknowledges the support from the National Science Council, Taiwan, under Contract NSC 91-2113-M-001-023. M.C.L. and Y.M.C. are grateful to Dr. J. Park for his preliminary optimization of the TS in Figure 7 and for the support of this work from the Basic Energy Sciences, Department of Energy, under Contract DE-FG02-97-ER14784, and the Cherry L. Emerson Center of Emory University for the use of its resources, which are in part supported by a National Science Foundation grant (CHE-0079627) and an IBM shared University Research Award. M.C.L. also acknowledges the support from the National Science Council for a Distinguished Visiting Professorship at National Chiao Tung University in Hsichu, Taiwan.

#### References and Notes

- Yu, T.; Lin, M. C. *J. Am. Chem. Soc.* **1993**, *115*, 4371.
- Lin, M. C.; Yu, T. *Int. J. Chem. Kinet.* **1993**, *25*, 875.
- Yu, T.; Lin, M. C. *J. Phys. Chem.* **1994**, *98*, 2105.
- Yu, T.; Lin, M. C. *Int. J. Chem. Kinet.* **1994**, *26*, 771.
- Yu, T.; Lin, M. C.; Melius, C. F. *Int. J. Chem. Kinet.* **1994**, *26*, 1095.
- Yu, T.; Lin, M. C. *J. Am. Chem. Soc.* **1994**, *116*, 9571.
- Yu, T.; Lin, M. C. *J. Phys. Chem.* **1995**, *99*, 8599.
- Tonokura, K.; Norikane, Y.; Koshi, M.; Nakano, Y.; Nakamichi, S.; Goto, M.; Hashimoto, S.; Kawasaki, M.; Andersen Sulbaek, M. P.; Hurley, M. D.; Wallington, T. J. *J. Phys. Chem. A* **2002**, *106*, 5908.
- McCoustra, M. R. S.; Pfab, J. *Chem. Phys. Lett.* **1985**, *122*, 395.
- Engert, J. M.; Slenczka, A.; Kensity, U.; Dick, B. *J. Phys. Chem.* **1996**, *100*, 11883.
- Bhujle, V.; Wild, U. P.; Baumann, H.; Wagniere, G. *Tetrahedron* **1976**, *32*, 467.
- Bhujle, V. V. *Spectrosc. Lett.* **1997**, *10*, 587.
- Chernoff, D. A.; Hochstrasser, R. M. *Chem. Phys. Lett.* **1980**, *70*, 213.
- Condirston, D. A.; Knight, A. R.; Steer, R. P. *J. Photochem.* **1980**, *14*, 257.
- Hatton, W. G.; Hacker, N. P.; Kasai, P. H. *J. Chem. Soc., Chem. Commun.* **1990**, 227.
- Niles, S.; Wight, C. A. *Chem. Phys. Lett.* **1989**, *154*, 458.
- Kessler, A.; Kensity, U.; Dick, B. *Chem. Phys. Lett.* **1998**, *289*, 516.
- Kessler, A.; Slenczka, A.; Seiler, R.; Dick, B. *Phys. Chem. Chem. Phys.* **2001**, *3*, 2819.
- Seiler, R.; Dick, B. *Chem. Phys.* **2003**, *288*, 43.
- Oberhuber, T. J.; Kensity, U.; Dick, B. *Phys. Chem. Chem. Phys.* **2003**, *5*, 2799.
- Li, Y. M.; Sun, J. L.; Han, K. L.; He, G. Z. *Chem. Phys. Lett.* **2001**, *338*, 297.
- Huang, J. H.; Wang, G. J.; Gu, X. B.; Han, K. L.; He, G. H. *J. Phys. Chem. A* **2000**, *104*, 10079.
- Tsai, S. T.; Lin, C. K.; Lee, Y. T.; Ni, C. K. *Rev. Sci. Instrum.* **2001**, *72*, 1963.
- Tsai, S. T.; Lee, Y. T.; Ni, C. K. *J. Phys. Chem. A* **2000**, *104*, 10125.
- Tsai, S. T.; Lin, C. K.; Lee, Y. T.; Ni, C. K. *J. Chem. Phys.* **2000**, *113*, 67.
- Tsai, S. T.; Huang, C. L.; Lee, Y. T.; Ni, C. K. *J. Chem. Phys.* **2001**, *115*, 2449.
- Becke, A. D. *J. Chem. Phys.* **1992**, *96*, 2155.
- Becke, A. D. *J. Chem. Phys.* **1992**, *97*, 9173.
- Becke, A. D. *J. Chem. Phys.* **1993**, *98*, 5648.
- Park, J.; Dyakov, I. V.; Mebel, A. M.; Lin, M. C. *J. Phys. Chem.* **1997**, *101*, 6043.
- Mebel, A. M.; Morokuma, K.; Lin, M. C. *J. Chem. Phys.* **1995**, *103*, 7414.
- Curtiss, L. A.; Redfern, P. C.; Raghavachari, K.; Pople, J. A. *J. Chem. Phys.* **2001**, *114*, 108.
- Bauernschmitt, R.; Ahlrichs, R. *Chem. Phys. Lett.* **1996**, *256*, 454.
- Stratmann, R. E.; Scuseria, G. E.; Frisch, M. J. *J. Chem. Phys.* **1998**, *109*, 8218.
- Casida, M. E.; Jamorski, C.; Casida, K. C.; Salahub, D. R. *J. Chem. Phys.* **1998**, *108*, 4439.

- (36) Frisch, M. J.; Trucks, G. W.; Schlegel, H. B.; Scuseria, G. E.; Robb, M. A.; Cheeseman, J. R.; Zakrzewski, V. G.; Montgomery, J. A., Jr.; Stratmann, R. E.; Burant, J. C.; Dapprich, S.; Millam, J. M.; Daniels, A. D.; Kudin, K. N.; Strain, M. C.; Farkas, O.; Tomasi, J.; Barone, V.; Cossi, M.; Cammi, R.; Mennucci, B.; Pomelli, C.; Adamo, C.; Clifford, S.; Ochterski, J.; Petersson, G. A.; Ayala, P. Y.; Cui, Q.; Morokuma, K.; Malick, D. K.; Rabuck, A. D.; Raghavachari, K.; Foresman, J. B.; Cioslowski, J.; Ortiz, J. V.; Baboul, A. G.; Stefanov, B. B.; Liu, G.; Liashenko, A.; Piskorz, P.; Komaromi, I.; Gomperts, R.; Martin, R. L.; Fox, D. J.; Keith, T.; Al-Laham, M. A.; Peng, C. Y.; Nanayakkara, A.; Gonzalez, C.; Challacombe, M.; Gill, P. M. W.; Johnson, B.; Chen, W.; Wong, M. W.; Andres, J. L.; Gonzalez, C.; Head-Gordon, M.; Replogle, E. S.; Pople, J. A. *Gaussian 98*, Revision A.7; Gaussian, Inc.: Pittsburgh, PA, 1998.
- (37) Amos, R. D.; Bernhardsson, A.; Berning, A.; Celani, P.; Cooper, D. L.; Deegan, M. J. O.; Dobbyn, A. J.; Eckert, F.; Hampel, C.; Hetzer, G.; Knowles, P. J.; Korona, T.; Lindh, R.; Lloyd, A. W.; McNicholas, S. J.; Manby, F. R.; Meyer, W.; Mura, M. E.; Nicklass, A.; Palmieri, P.; Pitzer, R.; Rauhut, G.; Schutz, M.; Schumann, U.; Stoll, H.; Stone, A. J.; Tarroni, R.; Thorsteinsson, T.; Werner, H.-J. MOLPRO, version 98.1; University of Birmingham: Birmingham, U.K., 1998.
- (38) Glassman, I. *Combustion*, 2nd ed.; Academic Press: New York, 1986.
- (39) Haynes, D. S. *Fossil Fuel Combustion*; Wiley-Interscience: New York, 1991.
- (40) Bockhorn, H. *Soot Formation in Combustion*; Springer-Verlag: New York, 1993.
- (41) Madden, L. K.; Moskaleva, L. V.; Kristyan, S.; Lin, M. C. *J. Phys. Chem. A* **1997**, *101*, 6790.
- (42) Braun-Unkoff, M.; Frank, P.; Just, T. *22nd Symp. (Int.) Combust.* **1988**, 1053.
- (43) Wang, H.; Laskin, A.; Moriaty, N. W.; Frenklach, M. *Proc. Combust. Inst.* **2000**, *28*, 1545.
- (44) (a) Wardlaw, D. M.; Marcus, R. A. *Chem. Phys. Lett.* **1984**, *110*, 230. (b) Wardlaw, D. M.; Marcus, R. A. *J. Chem. Phys.* **1985**, *83*, 3462.
- (45) (a) Klippenstein, S. J. *Chem. Phys. Lett.* **1990**, *170*, 71. (b) Klippenstein, S. J. *J. Chem. Phys.* **1991**, *94*, 6469.
- (46) Klippenstein, S. J. *J. Chem. Phys.* **1992**, *96*, 367.
- (47) Robertson, S. H.; Wagner, A. F.; Wardlaw, D. M. *J. Chem. Phys.* **1995**, *103*, 2917.
- (48) Klippenstein, S. J.; Wagner, A. F.; Dunbar, R. C.; Wardlaw, D. M.; Robertson, S. H. Variflex, version 1.00, July 16, 1999.
- (49) Varshni, Y. P. *Rev. Mod. Phys.* **1957**, *29*, 664.
- (50) Horn, C.; Frank, P.; Tranter, R. S.; Schaugg, J.; Grotheer, H.-H.; Just, T. *26th Symp. (Int.) Combust.* **1996**.
- (51) Choo, K.-L.; Golden, D. M.; Benson, S. W. *Int. J. Chem. Kinet.* **1975**, *7*, 713.
- (52) Lu, C.-W.; Wu, Y.-J.; Lee, Y.-P.; Zhu, R. S.; Lin, M. C. *J. Phys. Chem. A* **2003**, *107*, 11020.